5-12-95

SANDIA REPORT

SAND95–0500 • UC–404
Unlimited Release
Printed April 1995

Analysis of the Frequency Response of a TeO_2 Slow Shear Wave Acousto-Optic Cell Exposed to Radiation

Ireena A. Erteza

Prepared by
Sandia National Laboratories
Albuquerque, New Mexico 87185 and Livermore, California 94550
for the United States Department of Energy
under Contract DE-AC04-94AL85000

Issued by Sandia National Laboratories, operated for the United States Department of Energy by Sandia Corporation.

Printed in the United States of America. This report has been reproduced directly from the best available copy.

Available to DOE and DOE contractors from
Office of Scientific and Technical Information
PO Box 62
Oak Ridge, TN 37831

Prices available from (615) 576-8401, FTS 626-8401

Available to the public from
National Technical Information Service
US Department of Commerce
5285 Port Royal Rd
Springfield, VA 22161

NTIS price codes
Printed copy: A03
Microfiche copy: A01

SAND95-0500
Unlimited Release
Printed April 1995

Distribution
Category UC-404

Analysis of the Frequency Response of a TeO_2 Slow Shear Wave Acousto-Optic Cell Exposed to Radiation

Ireena A. Erteza
Optical Systems and Image Processing Department
Sandia National Laboratories
Albuquerque, NM 87185

Abstract

Radiation testing of photonic components is not new, however component level testing to date has not completely addressed quantities which are important to system behavior. One characteristic that is of particular importance for optical processing systems is the frequency response. In this report, we present the analysis of data from an experiment designed to provide a preliminary understanding of the effects of radiation on the frequency response of acousto-optic devices. The goal of the analysis is to describe possible physical mechanisms responsible for the radiation effects and to discuss the effects on signal processing functionality.

The experiment discussed in this report was designed by Sandia National Laboratories and performed by Sandia and Phillips Laboratory personnel at White Sands Missile Range (WSMR). In the experiment, a TeO_2 slow shear wave acousto-optic cell was exposed to radiation from the WSMR linear accelerator. The TeO_2 cell was placed in an experimental configuration which allowed swept frequency diffracted power measurements to be taken during radiation exposure and recovery. A series of exposures was performed. Each exposure consisted of between 1 to 800, 1 μsec radiation pulses (yielding exposures of 2.25 kRad(Si) to 913 kRad(Si)), followed by recovery time.

At low total and cumulative doses, the bandshape of the frequency response (i.e. diffracted power vs. frequency) remained almost identical during and after radiation. At the higher exposures, however, the amplitude and width of the frequency response changed as the radiation continued, but returned to the original shape slowly after the radiation stopped and recovery proceeded. It is interesting to note that the location of the Bragg degeneracy does not change significantly with radiation. In this report, we discuss these effects from the perspective of anisotropic Bragg diffraction and momentum mismatch, and we discuss the effect on the signal processing functionality.

35

Acknowledgements

This work supported by the Defense Nuclear Agency under WFO Proposal Number 91930113 and by the United States Department of Energy under Contract DE-AC04-94AL85000. The author acknowledges Ed Roos of Allied Signal for his help in obtaining reference material for this paper and Phillips Lab for their part in helping to conduct the experiments at WSMR.

Contents

List of Figures

List of Tables

1 Introduction

Optical processing has been around for more than a quarter of a century. Although it has not become universally accepted, optical processing has shown itself to be useful in a variety of situations. Some of the advantages of optical processing systems include high speed, a large capacity for handling data in parallel, compact and light weight systems, and low power. Recent improvements in various optical and optoelectronic devices are making optical processing even more attractive for certain applications. One of these applications is space-based optical processing, where size and power are critical. However, the effects of radiation are a concern for space applications and must be quantified.

The goal of this paper is to address the effect of radiation on acousto-optic cells being used in optical processing systems. To this end, an experiment was designed to measure the frequency response of an acousto-optic cell; the experiment, itself, is a very simple processing system–a spectrum analyzer.

A spectrum analyzer was chosen because it is a simple processing configuration, however, it contains virtually all the components that are in more complicated processing systems. The basic configuration of a spectrum analyzer is shown in Figure 1. [2] Its operation can be explained as follows.

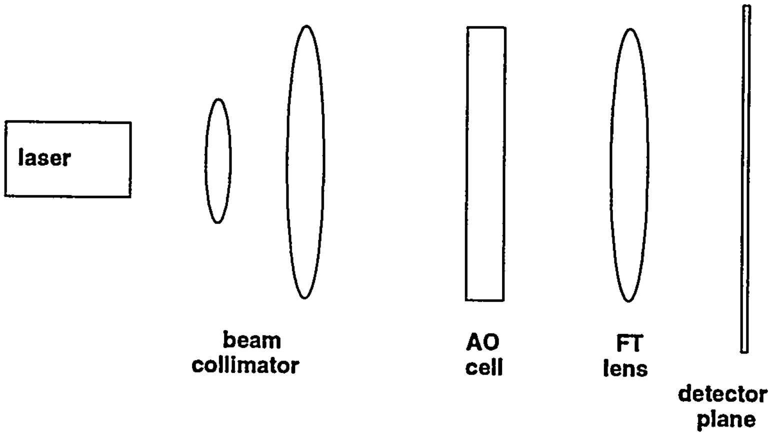

Figure 1: Basic Layout of a Spectrum Analyzer

Light from a laser is expanded and collimated to fill the aperture of an acousto-optic (AO) cell. The RF signal applied to the cell acts as a moving diffraction grating for the collimated light. The light is diffracted by the sound column at angles proportional to the frequency components of the RF signal supplied. The intensity at the different angles indicates the amount of RF power at that corresponding frequency. A lens can be placed behind the cell to capture and focus the light onto a detector array, located at what can be called the frequency plane. Since the diffracted angle out of the AO cell is proportional to the frequency, the various positions in the detector array correspond to various frequencies.

The behavior of such a spectrum analyzer can be described mathematically as follows. The collimated, expanded light source illuminates the AO cell with a spatial distribution $f(x)$. Typically, this distribution is a truncated gaussian. The RF input to the transducer creates a traveling acoustic wave inside the cell $aa(x - Vt)$, where V is the velocity of sound in the cell. The result of the acousto-optic interaction is proportional to $f(x)aa(x - Vt)$. The diffraction efficiency of the acousto-optic cell varies with the frequency of the acoustic wave inside the cell. Let this variation be described by $B(f_x)$, where f_x is the acoustic spatial frequency. The lens following the AO cell performs a fourier transform, such that the output, $O(x')$ is given by

$$O(x') = B(x') \cdot \left[F(x') * AA(x')e^{j2\pi x'Vt}\right] = B(x') \int_0^\infty f(\xi)aa(\xi - Vt)e^{-2\pi jx'\xi}d\xi, \quad (1)$$

where x' is the coordinate in the output plane. The term $e^{j2\pi x'Vt}$ is a Doppler shift, due to the velocity of sound. The output of the photodetector is then proportional to $|F(x') * AA(x')|^2$, assuming the Bragg frequency response of the AO cell, $B(f_x)$, is flat over the band of interest. Since the fourier transform of a broad function in time is narrow in frequency spectrum, it is clear that the frequency resolution of the system is limited by the aperture of the cell, which directly affects $f(x)$. Because optical processing is based on linearity and superposition, the frequency response of AO cells is of critical concern.

It is important to realize that what we are calling the frequency response of the AO spectrum analyzer is not a simple transfer function in the linear systems sense. Because the fourier transform operation performed by the AO spectrum analyzer is linear, but *not* invariant, there is no transfer function for this system in the usual sense.

Still, the performance of the AO spectrum analyzer does depend on the frequencies of the input signal, the spatial frequencies of the input light and on how the diffraction efficiency of the AO cell varies with acoustic frequency, and so there is a "frequency response" associated with this system. This can be seen by looking at the block diagram in Figure 2. The frequency response of an acousto-optic device is limited by both the Bragg frequency response, $B(s)$, and the transducer frequency response, $T(s)$. The shapes of $T(s)$, $f(x)$ and $B(s)$ affect the spectral resolution of the AO spectrum analyzer as follows.

- The transducer frequency response is multiplied by the spectrum of the original signal. Equivalently, the impulse response of the transducer is convolved with the input signal $a(t)$. If the bandshape of the transducer frequency response is bandlimited, the net effect is to broaden the acoustic signal in time. We refer to this post-transducer signal as $aa(x)$, since the transducer also converts the time varying signal to a space varying signal.
- In the AO cell, the light signal and the post-transducer acoustic signal are multiplied. The output signal in space is proportional to this product, convolved with the impulse response of the Bragg frequency response. Recall that the Bragg diffraction efficiency of the cell varies with spatial frequency.

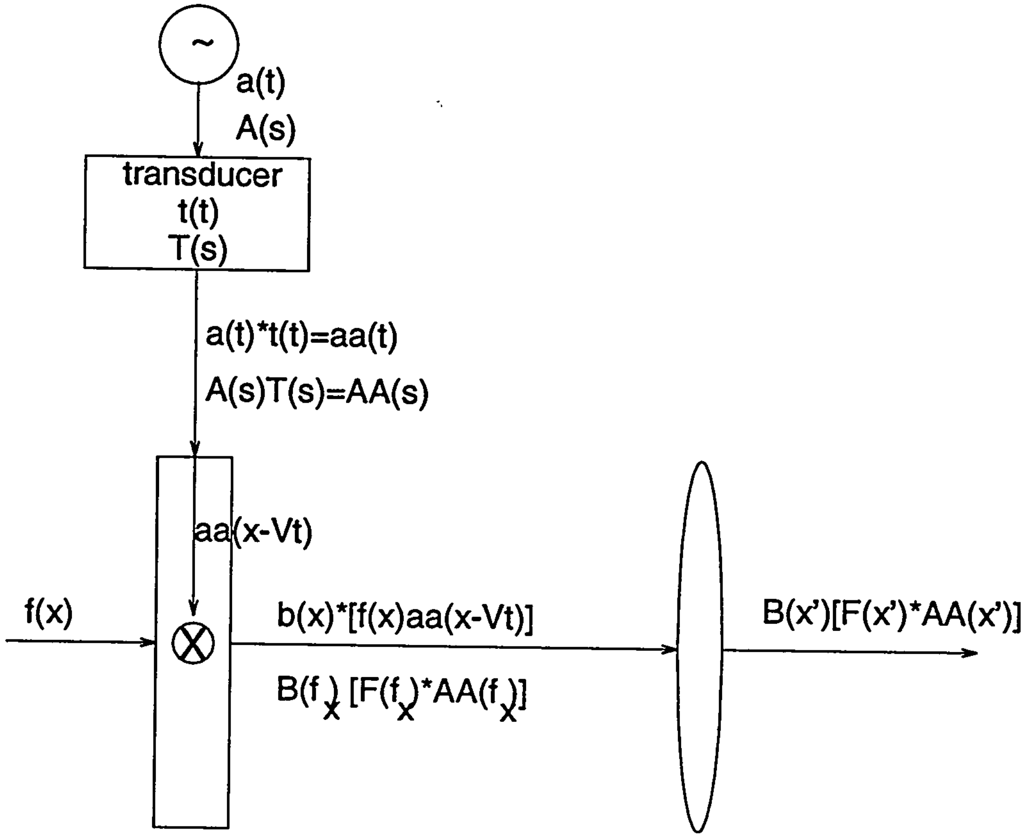

Figure 2: Block Diagram of an Acousto-Optic Spectrum Analyzer

We call this $B(f_x)$. Therefore in the spatial frequency domain, the output of the cell is $B(f_x) \cdot [F(f_x) * AA(f_x)]$.

Notice that the spectrum of the post-transducer acoustic signal is smeared by convolution with the spectrum of the light signal. Typically, the light signal is either a rectangle function or a truncated gaussian. The finite duration of $f(x)$ leads to a limit in spectral resolution. However, the actual shape of $f(x)$ can serve as a windowing function to improve resolution, or peak-to-sidelobe ratio, slightly.

The output from the AO cell in the spatial frequency domain can be found in two steps: (1) convolve the spectrum of the light signal with the spectrum of the post-transducer acoustic signal; and (2) multiply that resultant spectrum by $B(f_x)$. Note that $B(f_x)$ multiplies $[F(f_x) * AA(f_x)]$; it is not convolved with it. This means that the amplitude of $[F(f_x) * AA(f_x)]$ will be altered, but the spectral resolution will not be affected if $B(f_x)$ is reasonably smooth.

- Finally, the fourier transform lens brings the spatial frequency domain into the spatial domain, so that what is measured as a function of x', the variable in the output plane, is $B(x') \cdot [F(x') * AA(x')]$.

The two functions, $T(s)$ and $B(f_x)$ cannot be combined into one effective transfer function for the entire system.

2 Experimental Configuration

SNL has a project with the Defense Nuclear Agency (DNA) called Radiation Effects on Optical Processing Systems (REOPS). The goal of this project is to relate component level radiation effects to system level performance through modeling and testing of a selected optical processing system. This goal requires the identification of a "generic" architecture which incorporates key features of most optical processing systems to serve as a basis for the modeling effort. The acousto-optic spectrum analyzer architecture described previously was chosen as a prototypical optical processing system, because it has all the major components of most optical processing systems. With the test system chosen, work proceeds toward the project goal: to test the behavior of the individual components exposed independently to radiation and determine how those radiation effects can affect system performance. The acousto-optic cell is critical to many acousto-optic processing systems, hence we are concentrating on the effects on this component first.

The experimental configuration for the prototypical optical system (acousto-optic spectrum analyzer) is shown in Figure 3. The parts in this figure are numbered, and the numbers refer to the items listed in Table 2.

Light is provided by a HeNe laser with a neutral density filter. The output power after the filter is 580μW. A special mount for the AO cell was built. The mount enables rotation about the acoustic axis (y-axis [110]) and about the x-axis running perpendicular to the plane including [110] and the optical rail path. A stop is placed on the cylindrical lens to block out the DC and negative diffraction orders. The tilt of the detector face is very critical, because at certain angles, the face of the detector can send a reflected beam back into the laser, altering the beam characteristics.

Part No.	Item Description
1	Uniphase 1135P HeNe laser, 20 mW, linearly polarized
2	NRC 811 laser mount
3	NRC 370 post assembly
4	counterweight
5	1.47 neutral density filter, reflective type
6	Oriel Dog to secure plate to optical rail
7	Newport #38 plate (12.6cm X 7.5 cm)
8	Newport linear translator stage
9	Newport 360-90 triangle bracket
10	Newport 481 series rotary stage
11	Custom mount for AO cell
12	AO cell
13	Melles Griot 78803 #10 cylindrical lens; focal length 150 mm
14	Melles Griot 10 nm bandpass interference filter centered at 632.8 nm
15	UDT Pin 10 silicon detector, 1 cm in diameter

Table 1: Optical Parts

Figure 4 shows the corresponding electronics for this experiment. The numbered parts are listed in Table 2. The electronic spectrum analyzer and oscilloscope were used for monitoring purposes; they are not part of the AO spectrum analyzer system. Measurements were taken to quantify the frequency response of the various

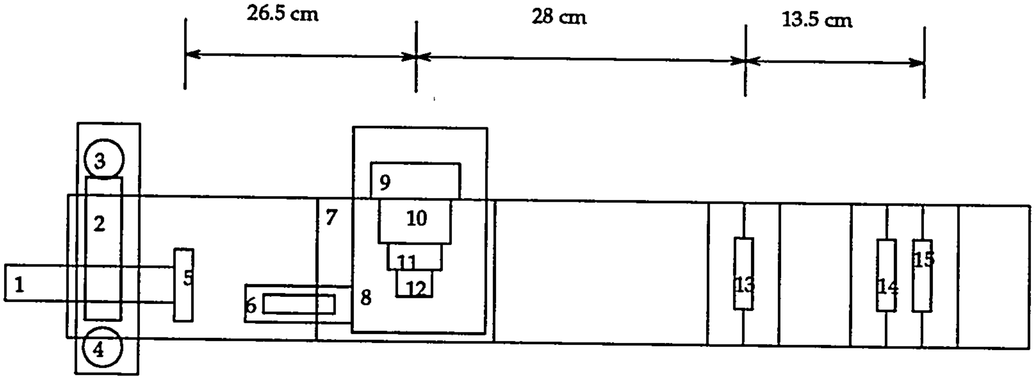

Figure 3: Top View of Experiment on an Optical Rail

Part No.	Item Description
4	Wavetek Model # 134 Sweep Generator
5	HP 8620C Sweep Oscillator
6	Tektronix 7854 Oscilloscope
7	6dB RF attenuator
8	MiniCircuits 50-50 splitter
9	Tektronix 496P Programmable Spectrum Analyzer
10	BK Precision DC power supply; 30V, 1 ampere
11	MiniCircuits ZHL-2-8 RF Power Amplifier
12	MiniCircuits 50-50 splitter
13	10dB RF attenuator
14	HP 8482A Power Sensor
15	HP 436A Power Meter
16	Melles Griot Large Dynamic Amplifier

Table 2: Electrical Parts

RF amplifiers. The RF amplifiers used in this experiment were chosen to have a reasonably flat response in the band of interest. The variations in the band of interest were within 10% for all the amplifiers used.

The configuration in Figures 3 and 4 was designed, built and tested in a radiation free environment at Sandia. Testing included checking the general operation of the system and characterization of the system. In addition, the acousto-optic interaction plane was rotated to give a flat, wide frequency response, with the location of the Bragg degeneracy clearly visible. The RF frequency was swept from 12–65 MHz. RF power was 400 mW. Nominal characteristics for the Crystal Tech AO cell are 30 MHz bandwidth, centered at 50 MHz, with a 70μsec time aperture. The clear aperture measures 12 mm X 43.5 mm. Once this testing was done, with the system robustly mounted on a portable optical rail, the experiment was taken to WSMR and exposed to radiation. Care was taken to isolate the radiation to expose only the crystal material itself, and not the transducer or any other part of the system.

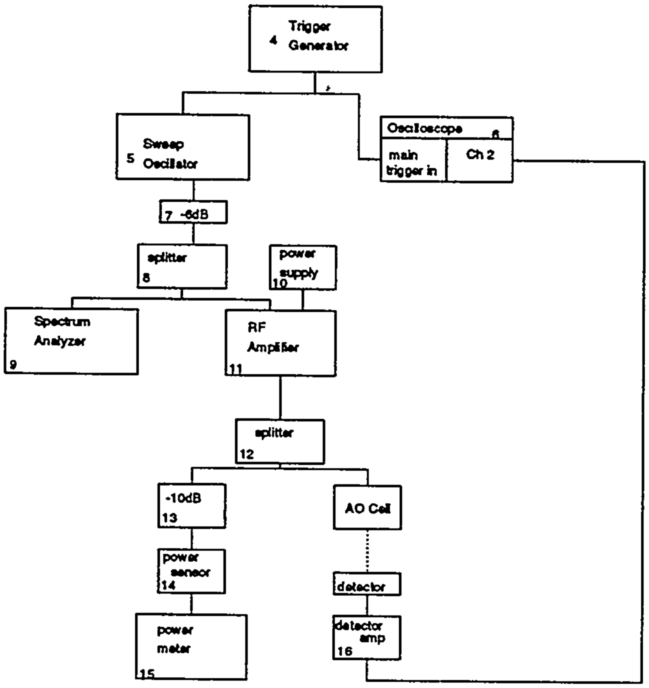

Figure 4: Block Diagram of Electronics

3 Review of the Theory of Anisotropic Bragg Diffraction

The data from this experiment shows the effect of radiation on the frequency response of a TeO_2 slow shear wave crystal. In order to better interpret the data, let us first briefly review the basic theory of anisotropic Bragg diffraction.

3.1 Qualitative Review

In an acousto-optic cell, incident light is diffracted by an effective grating produced by a sound column in the cell. The interaction between the light and sound is governed by pseudomomentum conservation, that is

$$\vec{k_i} + \vec{K} = \vec{k_d} \tag{2}$$

$$\nu_i = \nu_d \pm f_a \tag{3}$$

$$|k| = \frac{2\pi\nu}{c} = \frac{2\pi n}{\lambda} \tag{4}$$

$$k_i = \frac{2\pi n_i}{\lambda_o} \tag{5}$$

$$k_d = \frac{2\pi n_d}{\lambda_o} \tag{6}$$

$$K = \frac{2\pi}{\Lambda} = \left(\frac{2\pi}{V}\right) f_a, \tag{7}$$

where $\vec{K}$ is the acoustic k-vector, $\vec{k_i}$ is the incident optical k-vector, and $\vec{k_d}$ is the diffracted optical k-vector. V is the acoustic velocity, Λ is the acoustic wavelength and f_a is the acoustic frequency. λ_o is the optical wavelength, and ν_i and ν_d are the incident and diffracted optical frequencies.

For isotropic Bragg diffraction, there is only one index of refraction for the crystal, so that $|\vec{k_i}| = |\vec{k_d}|$, and essentially the angle of incidence is equal to the angle of diffraction. For an anisotropic crystal, however, there are two indices of refraction. For a longitudinal acoustic wave, the polarization of the incident light is the same as the diffracted, so the interaction is analogous to the isotropic case. In a shear acoustic wave, however, the displacement of matter is perpendicular to the direction of propagation of the acoustic wave, and the polarization of the diffracted light is rotated by 90°. Therefore, the matching of the momentum vectors takes place between two ellipses, representing the two different polarizations. This is illustrated in Figure 5.

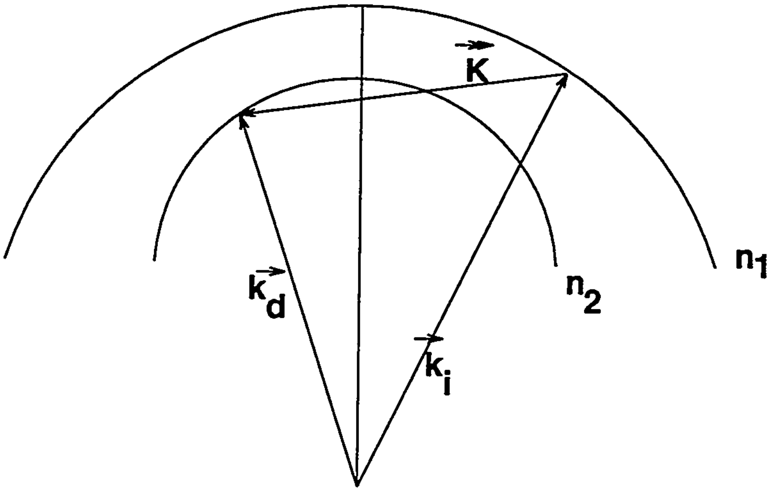

Figure 5: Psuedomomentum Diagram for Anisotropic Bragg Diffraction

In a standard slow shear orientation for TeO_2, the acoustic wave propagates down the [110] crystal axis. This mode has a very slow acoustic velocity compared to most materials, resulting in a long time aperture and a high acousto-optic figure of merit. The acousto-optic figure of merit is directly related to the diffraction efficiency and will be discussed in detail later. The optical interaction plane typically is the plane containing [110] (the acoustic direction of propagation) and [001] (the optical axis), with light propagating down [001].

TeO_2 is not just an anisotropic material, it is also optically active. As a result, there are not only two linear polarizations with different indices of refraction, but left- and right-handed circular polarizations have different indices too. The index splitting is much smaller for the circular polarizations, resulting in a more useful frequency range over which pseudomomentum matching occurs. However, to take advantage of this desired frequency range requires elliptically polarized optical input modes. If linear polarized modes are used, the diffraction efficiency will by approximately 50% of the value when the correct polarization is used. [7] As a result, an additional optical component, a quarter wave plate, should be used to maximize the diffraction efficiency.

There is another solution, however. If the optical interaction plane is rotated about the [110] axis, so that it now contains [110], but not the optical axis [001], the elliptical polarization requirements can be mitigated, and the input and diffracted optical beams can have almost linear polarizations. This has several significant benefits. First, an additional component is not needed in the system, resulting in less weight and fewer alignment considerations. Also, unwanted scattered light can now be reduced by positioning an analyzer after the Bragg cell. This might add an additional component, but can improve the SNR. Finally, the overall diffraction efficiency can increase.

The main benefit of optical rotation, however, is that the geometry is altered to allow tangential phase matching. In tangential phase matching, the acoustic wave vector is perpendicular to the diffracted or incident beam. This is illustrated in Figure 6. However, tangential phase matching can occur in non-rotated geometries, as well.

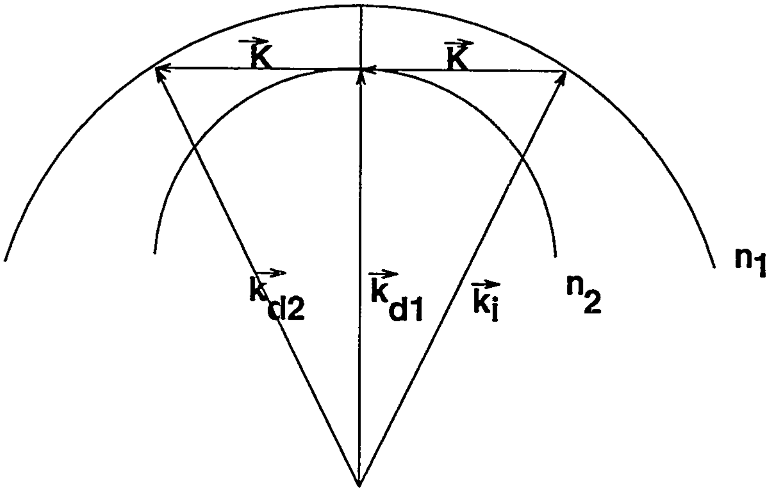

Figure 6: Pseudomomentum Diagram for Tangential Phase Matching

Tangential phase matching is desired because in the tangential phase matching geometry, the maximum effective transducer length is achieved. [8] The diffraction efficiency is directly proportional to the effective transducer length, so maximizing L maximizes the diffraction efficiency.

There are tradeoffs associated with tangential phase matching. For example, tangential phase matching restricts the optical range for the device, since the center frequency varies with the wavelength.

There is an additional undesired effect associated with the tangential phase matching. If the fast mode of light is incident upon the acoustic wave vector, such that the diffracted beam is in the slow mode and is perpendicular to the acoustic wave vector, a degeneracy occurs at a certain frequency. The degeneracy means that there are two angles which satisfy the pseudomomentum conservation. As a result, some light is deflected into the undesired, degenerate mode, causing a dip in the diffraction efficiency at the given frequency. There is usually some divergence associated with the acoustic wave, which gives the dip a certain width. This is a phenomenon associated with tangential phase matching, not optical rotation, so midband degeneracy occurs in other non-rotated configurations, as well.

This qualitatively describes the anisotropic Bragg diffraction process. There are equations that quantitatively describe this same process. We will include some of the quantitative descriptions, now, so that as we look at the results of the experiments, we can quantitatively understand and possibly explain the underlying physical mechanisms responsible.

3.2 Quantitative Review

This quantitative review is not meant to be exhaustive. Please see the mentioned references for more detail.

3.2.1 Dixon's Equations and the Bragg Degeneracy

If we consider θ_1 to be the incident beam angle, and θ_2 to be the diffracted beam angle, Dixon's equations describe the relationship between these angles, the refractive indices of the various modes and the acoustic frequency. [25]

$$\sin\theta_1 = \frac{\lambda}{2n_1\Lambda}\left(1 + \frac{\Lambda^2}{\lambda^2}(n_1^2 - n_2^2)\right) \tag{8}$$

$$\sin\theta_2 = \frac{\lambda}{2n_2\Lambda}\left(1 + \frac{\Lambda^2}{\lambda^2}(n_2^2 - n_1^2)\right), \tag{9}$$

where $n_1 = n_1(\theta)$ and $n_2 = n_2(\theta)$ are the indices of refraction of the two modes traveling in the θ direction.

In Figure 7, θ_1 and θ_2 are plotted versus frequency. The location of the minima in θ_1, gives the location in frequency of the Bragg degeneracy. The location, f_0 is given by the following equation, derived by setting the derivative of θ_1 to zero.

$$f_0 = \left(\frac{V}{\lambda}\right)\sqrt{n_1^2(\theta_0) - n_2^2(0)}, \tag{10}$$

where θ_0 is the minimum value for θ_1, $\sin\theta_0 = \frac{\lambda f_0}{n_1 V}$, and V is the velocity of sound.

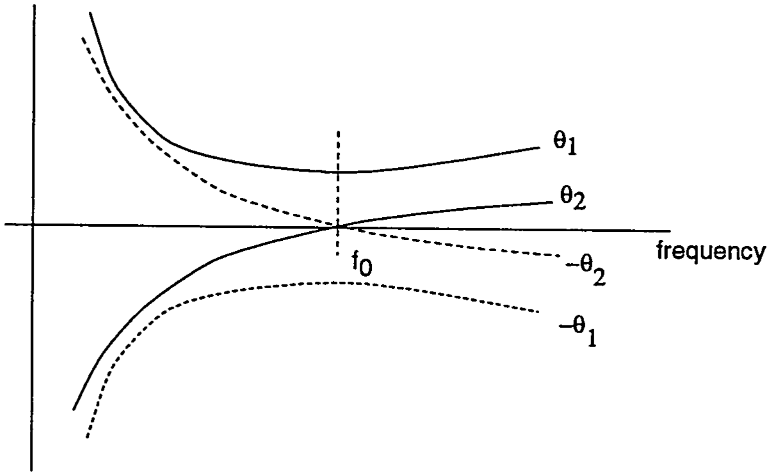

Figure 7: Pseudomomentum Diagram for Tangential Phase Matching

The location of f_0, also sometimes called f_c (center frequency), depends on the difference between the index of refraction of the two modes. These two modes can be linearly polarized modes (ordinary and extraordinary modes), or they can be left-handed and right-handed circularly polarized modes. The splitting between the indices of LH and RH circularly polarized modes is much smaller than between the linearly polarized modes, bringing the location for Bragg matching into a lower (and more useful) frequency range.

3.2.2 Optical Rotation

If $n_1(\theta)$ and $n_2(\theta)$ are the ordinary and extraordinary indices of refraction (for the circularly polarized modes of a birefringent crystal), n_o and n_e are the indices for the linearly polarized ordinary and extraordinary rays, and θ is the angle from the optic axis in which direction light is propagating, then the following approximation can be made for small θ [25]

$$n_1^2 = n_0^2(1 + 2\delta\cos^2\theta + \frac{n_e^2 - n_o^2}{n_e^2}\sin^2\theta) \tag{11}$$

$$n_2^2 = n_0^2(1 - 2\delta\cos^2\theta), \tag{12}$$

where $\delta = [n_1(0) - n_2(0)]/(2n_0)$.

Using Eqns. 11 and 12 into Dixon's equations, and neglecting terms in $\delta\sin^2(\theta)$ and $\sin^4(\theta)$,

$$\sin\theta_1 \approx \frac{\lambda}{2n_o\Lambda}\left[1 + \frac{4n_o^2\Lambda^2}{\lambda^2}\delta + \frac{\sin^2(\theta_1)\Lambda^2 n_o^2}{\lambda^2}\left(\frac{n_e^2 - n_o^2}{n_e^2}\right)\right] \tag{13}$$

$$\sin\theta_2 \approx \frac{\lambda}{2n_o\Lambda}\left[1 - \frac{4n_o^2\Lambda^2}{\lambda^2}\delta - \frac{\sin^2(\theta_1)\Lambda^2 n_o^2}{\lambda^2}\left(\frac{n_e^2 - n_o^2}{n_e^2}\right)\right], \tag{14}$$

where θ_1 is the angle observed inside the crystal.

Now, if the plane of acousto-optic interaction is rotated an angle Ψ from the z axis [001], about the y axis [110], then we can define η as the angle between the ray of light and the z axis as

$$\cos \eta_{1,2} = \cos \Psi \cos \theta_{1,2} \tag{15}$$

or

$$\eta_{1,2}^2 = \theta_{1,2}^2 + \Psi^2, \tag{16}$$

where $\theta_{1,2}$ are the Bragg angles for the two modes of light. See Figure 8.

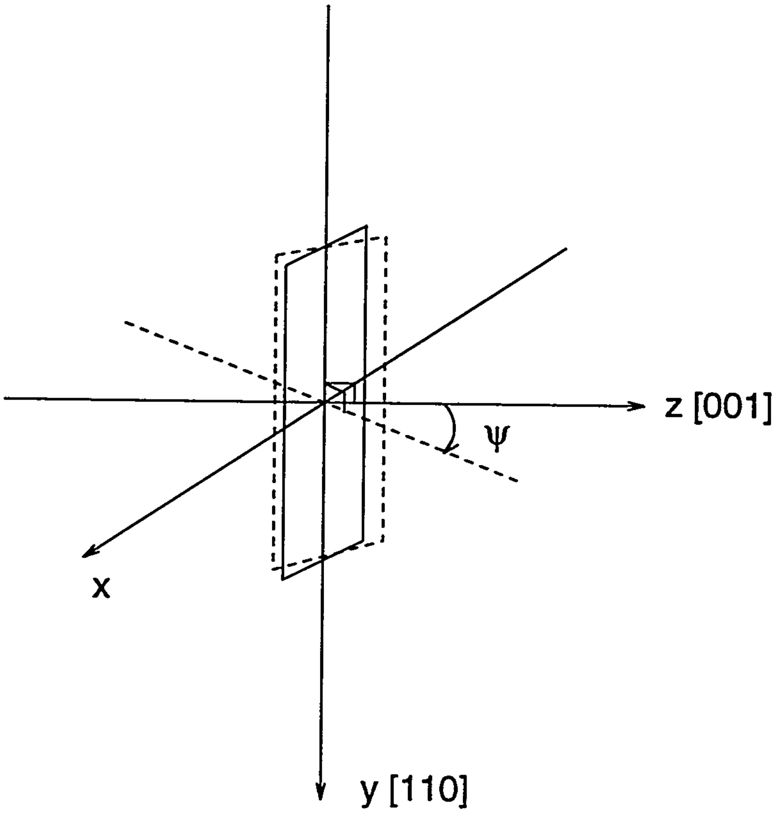

Figure 8: Geometry Showing Acousto-optic Plane of Interaction

Replacing θ by η in Eqns. 11 and 12, and using $\delta \rightarrow \frac{n_e^2-n_o^2}{n_e^2}$, gives us a new equation for the minimum of θ_1

$$f_0 = \frac{V}{\lambda}\left[2\delta \cos \Psi(\cos \theta_1 + \cos \theta_2) + \frac{n_e^2 - n_o^2}{n_e^2} \sin^2(\eta_1)\right]^{\frac{1}{2}}. \tag{17}$$

Therefore, if the deflector is rotated around the [110] direction of propagation of the sound wave, then the midband frequency, f_0 can be varied.

3.2.3 Coupled Mode Theory, Diffraction Efficiency and 3-dB Bandwidth

Acousto-optic interaction for both birefringent and isotropic media can be described by coupled mode interactions. Details on deriving and solving these coupled mode equations can be found a number of places. [26, 3, 25, 19, 14] Here we outline the specifics for birefringent diffraction, as detailed in Reference [26].

We are interested only in the Bragg regime, so the only two orders that need to be accounted for are $E_0(z)$ and $E_1(z)$. For the geometry given in Figure 9, the coupled mode equations involving the strain, S, and the effective acousto-optic coefficient, p, are:

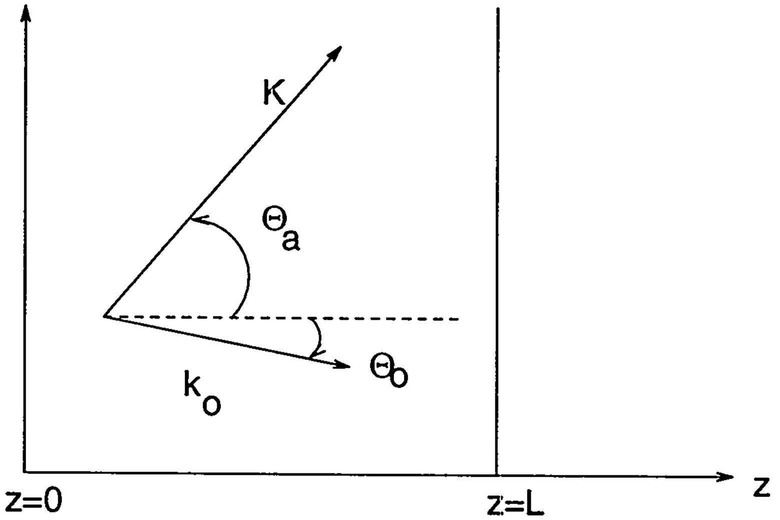

Figure 9: Basic Interaction Geometry

$$\frac{dE_0(z)}{dz} = -\frac{k_0^2 n_1^2}{4k'_{0z}} pSE_1(z) \tag{18}$$

$$\frac{dE_1(z)}{dz} - j\Delta k_1 E_1(z) = \frac{k_1^2 n_0^2}{4k'_{1z}} pSE_0(z), \tag{19}$$

where

$$\Delta k_m = \frac{k'^2_m - k^2_m}{2k'_{mz}} = \frac{k_0}{2c_m}\left[1 - \frac{n_m^2}{n_0^2} + 2m\frac{K}{k_0}\cos(\theta_a + \theta_o) + m^2\frac{K^2}{k_0^2}\right], \tag{20}$$

$$c_m = \cos\theta_o + \frac{mK}{k_0}\cos\theta_a, \tag{21}$$

and $k'_{mz} = c_m k_0$. In addition, $\mathbf{k}'_m$ is the diffracted optical vector, $\Delta\mathbf{k}_m$ lies parallel to the z axis, and $\mathbf{k}_m + \Delta\mathbf{k}_m = \mathbf{k}'_m$. This is illustrated in Figure 10. n_m is the refractive index associated with the m^{th} order mode.

Because we are interested in only describing the Bragg regime, Δk_1 is very small. As a result,

$$k'_{0z} \equiv k_{0z} = k_0 \cos\theta_0 \tag{22}$$

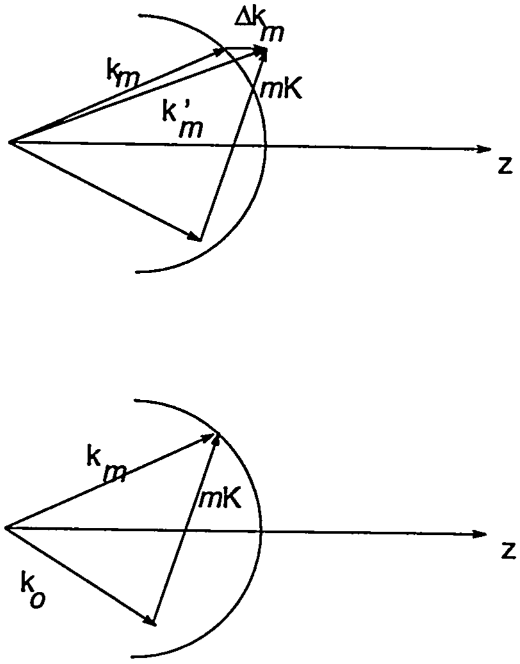

Figure 10: Illustration of Phase Mismatch and Exact Phase Matching.

$$k'_{1z} \approx k_{1z} = k_1 \cos\theta_1. \tag{23}$$

Incorporating the following definitions

$$\begin{aligned}
\Delta n_0 &\equiv -\frac{1}{2} n_0^2 n_1 p S \\
\Delta n_1 &\equiv -\frac{1}{2} n_1^2 n_0 p S \\
v_0 &\equiv -\frac{\omega_1}{c} \frac{\Delta n_0 L}{\cos\theta_1} \approx -\frac{2\pi}{\lambda_0} \Delta n_0 L \\
v_1 &\equiv -\frac{\omega_0}{c} \frac{\Delta n_1 L}{\cos\theta_0} \approx -\frac{2\pi}{\lambda_0} \Delta n_1 L \\
\zeta &\equiv -\frac{1}{2} \Delta k_1 L,
\end{aligned} \tag{24}$$

Eqns 18 and 19 can be rewritten as

$$\frac{dE_0(z)}{dz} = -\frac{v_1}{2L} E_1(z) \tag{25}$$

$$\frac{dE_1(z)}{dz} + j\frac{2\zeta}{L} E_1(z) = \frac{v_0}{2L} E_0(z). \tag{26}$$

Applying the following boundary conditions,

$$E_0(0) = E_0$$

$$E_0'(0) = 0$$

$$E_1(0) = 0$$

$$E_1'(0) = \frac{v_0}{2L} E_0, \tag{27}$$

the following differential equations can be written

$$E_0''(z) + j\frac{2\zeta}{L} E_0'(z) + \frac{v_0 v_1}{4L^2} E_0(z) = 0 \tag{28}$$

$$E_1''(z) + j\frac{2\zeta}{L} E_1'(z) + \frac{v_0 v_1}{4L^2} E_1(z) = 0. \tag{29}$$

The differential equations are solved, giving

$$E_0(z) = E_0 \exp\left[-j\frac{\zeta z}{L}\right]\left[\cos\frac{\sigma z}{L} + j\frac{\zeta}{\sigma}\sin\frac{\sigma z}{L}\right] \tag{30}$$

$$E_1(z) = E_0 \exp\left[-j\frac{\zeta z}{L}\right]\left(\frac{v_0}{2\sigma}\right)\sin\frac{\sigma z}{L}, \tag{31}$$

where

$$\sigma^2 \equiv \zeta^2 + \frac{v_0 v_1}{4}. \tag{32}$$

Incorporating one more definition,

$$v \equiv \sqrt{v_0 v_1}, \tag{33}$$

an equation for diffraction efficiency can be written as

$$\eta \equiv \frac{|E_1(L)|^2}{|E_0(0)|^2} = \left(\frac{v_0}{2}\right)^2\left(\frac{\sin\sigma}{\sigma}\right)^2 \approx \left(\frac{v}{2}\right)^2\left(\frac{\sin\sigma}{\sigma}\right)^2, \tag{34}$$

where

$$\sigma^2 \equiv \zeta^2 + \left(\frac{v}{2}\right)^2. \tag{35}$$

Note that diffraction efficiency and diffracted power differ only by a multiplicative constant.

It is often useful to relate the diffraction efficiency (or the diffracted power) to acoustic power, P_a. The average energy flow or acoustic power is given by the average energy flow density times the area of the acoustic beam (or equivalently the effective transducer area). The average energy density of an acoustic wave is related to the strain, S, and elastic stiffness constant, c, as $\frac{cS^2}{2}$. The elastic stiffness constant is equal to the mass density multiplied by the square of the acoustic wave velocity, $c = \rho V^2$. Multiplying the average energy density by the acoustic wave velocity, V gives the average energy *flow* density, $\rho V^3 S^2/2$. Finally, we can write the acoustic power as

$$P_a = \frac{\rho V^3 S^2 H L}{2}, \tag{36}$$

where H and L are the height and length of the acoustic beam.

Incorporating this information into the equations for v, we get

$$v = \frac{2\pi}{\lambda_0} \frac{1}{\cos\theta} \sqrt{P_a \frac{M_2 L}{2H}}, \tag{37}$$

or

$$\left(\frac{v}{2}\right)^2 = \left(\frac{\pi}{\lambda_0} \frac{1}{\cos\theta}\right)^2 P_a \frac{M_2 L}{2H}, \tag{38}$$

where

$$M_2 = \begin{cases} \frac{n^6 p^2}{\rho V^3} & \text{for isotropic diffraction} \\ \frac{n_0^3 n_1^3 p^2}{\rho V^3} & \text{for birefringent diffraction.} \end{cases} \tag{39}$$

If there is no phase mismatch, $\zeta = -\Delta k_1/2L = 0$, and $\eta = \sin^2(\frac{v}{2})$ is the peak intensity of the diffracted beam. Typically, $\zeta^2 \gg \left(\frac{v}{2}\right)^2$, so the following simplification is allowed:

$$I_1 = I_{1p} \mathrm{sinc}^2 \left(\frac{\Delta k_1 L}{2\pi}\right), \tag{40}$$

where $I_{1p} = \sin^2(\frac{v}{2})$ and $\mathrm{sinc}x = \frac{\sin \pi x}{\pi x}$.

Recall, the term $\left(\frac{\Delta k_m L}{2\pi}\right) = \delta_m$ can be considered the phase mismatch for the order m. For the birefringent case, it can be given more explicitly as [3]

$$\delta_1 = \frac{L}{2 n_0 \lambda_o c_1} \left[(n_0^2 - n_1^2) + 2 \frac{n_0 \lambda_o}{\Lambda} \cos(\theta_a + \theta_0) + \frac{\lambda_o^2}{\Lambda^2} \right]. \tag{41}$$

Recalling $c_m = \cos\theta_o + m\frac{k_a}{k_o}\cos\theta_a$, $f_c = \frac{V}{\lambda_o}\sqrt{n_1^2 - n_2^2}$ and assuming $\theta_a = 90°$

$$\delta_1 = \frac{L}{2L_o} \left[F^2 - 2\left(\frac{n_o \Lambda_o}{\lambda_0} \sin\theta_o\right) F + 1 \right], \tag{42}$$

where $L_o = \frac{n_0 \Lambda_o^2 \cos\theta_o}{\lambda_o}$ and $F = \frac{f}{f_c}$.

When $\sin\theta_o = \frac{\lambda_o}{n_o \Lambda_o}$ to satisfy the momentum matching conditions at $f = f_c$, then

$$\delta_1 = \frac{L}{2L_o} (F - 1)^2. \tag{43}$$

The 3-dB bandwidth is found by realizing that $\mathrm{sinc}^2 x = 0.5$, for $x = \pm 0.45$. Letting $\delta_1 = \pm 0.45$ gives

$$F_L = 1 - \sqrt{\frac{0.9 L_o}{L}}$$

$$F_H = 1 + \sqrt{\frac{0.9 L_o}{L}}$$

or

$$\frac{\Delta f}{f_c} = \sqrt{\frac{3.6 L_o}{L}}. \tag{44}$$

3.2.4 Resolution and Time Bandwidth Product

Finally, it is important to include a few equations relating to the number of resolvable points and the bandwidth of the device. [2, 12] Assuming that λ is the wavelength of light, and D is the beam diameter, the angular spread of the beam is given by $\frac{\lambda}{D}$. The number of resolvable elements, N, is given by

$$N = \frac{\Delta\theta D}{\lambda}, \tag{45}$$

where $\Delta\theta$ is the maximum deflection angle. If the maximum bandwidth of the device is Δf, the maximum deflection angle is given by

$$\Delta\theta = \frac{\lambda\Delta f}{V}. \tag{46}$$

Combining these facts, and realizing the transit time across the cell is given by

$$\tau = \frac{D}{V}, \tag{47}$$

gives

$$N = \tau\Delta f. \tag{48}$$

N is also known as the time bandwidth product.

4 Experimental Results

This section shows plots of the experimental results. The radiation source was from the WSMR Linac. The energy of the electron beam was nominally 15 MeV, and the pulse duration of each pulse was 1 μsec. The pulse repetition rate was 30 Hz, or equivalently every 33 msec. Dosimeters were place to get a dose reading in kRad (Si), and thermistors were place to monitor the temperature variation of the cell. Dose size increased with exposure number, as seen in Table 4.

Data traces from the various exposures are shown in Figures 4 through 27. On the plot legends, the numerical indices refer to the trace number. For example, Diff_10 refers to the tenth trace taken during that exposure. Traces were taken sequentially during and after radiation.

Figures 28 through 38 show how the temperature varies with radiation and recovery for the various exposures. On these figures, time equals zero corresponds to the first radiation pulse. The temperature immediately starts to fall after the last radiation pulse.

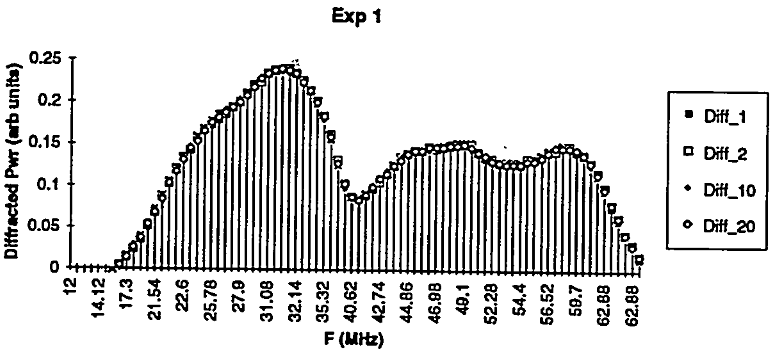

Figure 11: Exposure 1: Trace 1 was after the first and only radiation pulse. Traces 2, 10 and 20 were during the recovery period.

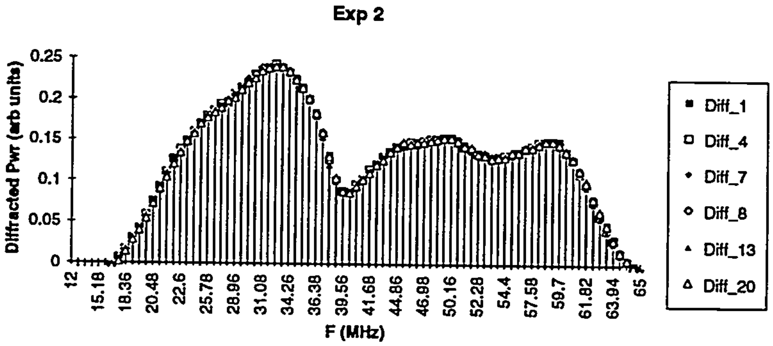

Figure 12: Exposure 2: Traces 1, 4 and 7 were during radiation. Traces 8, 13 and 20 were during recovery.

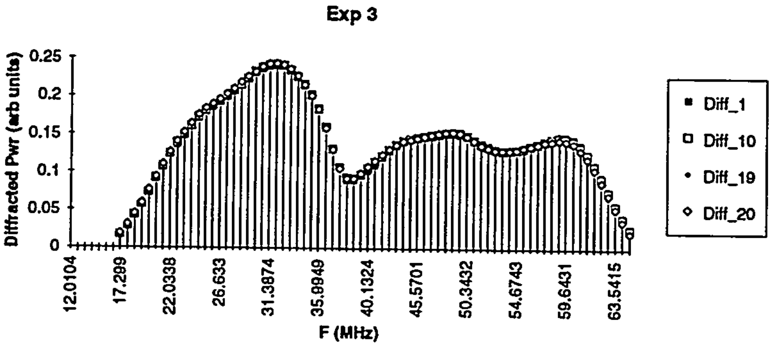

Figure 13: Exposure 3: Traces 1, 10 and 19 were during radiation. Trace 20 was during recovery.

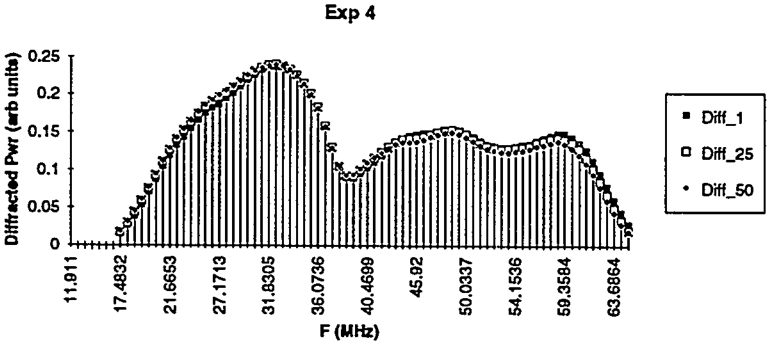

Figure 14: Exposure 4, Plot 1: Traces 1, 25 and 50 were during radiation.

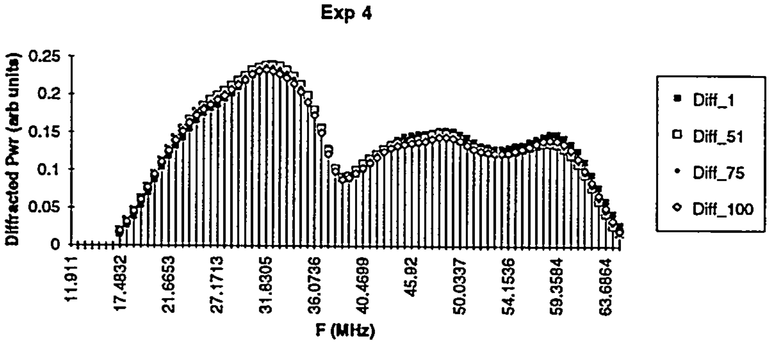

Figure 15: Exposure 4, Plot 2: Traces 51, 75 and 100 were during recovery.

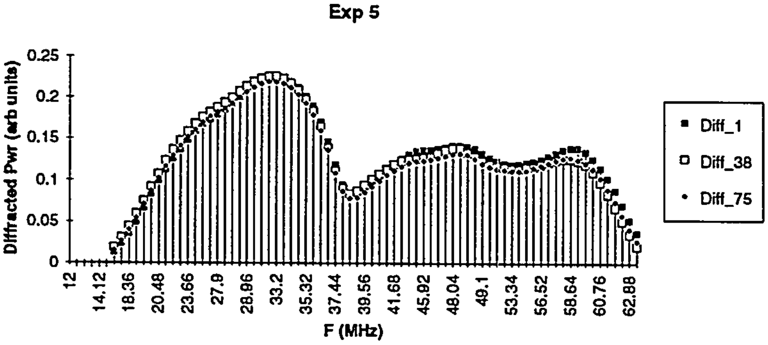

Figure 16: Exposure 5, Plot 1: Traces 1, 38 and 75 were during radiation.

Exposure #	# Pulses	Dose (kRad (Si))	Cumulative Dose (kRad (Si))
1	1	2.25	2.25
2	5	11.25	13.5
3	20	40.9	54.4
4	50	95.1	149.5
5	75	79.9	229.4
6	100	105.4	334.8
7	100	157.5	492.3
8	200	209.2	701.5
9	400	434.0	1144.0
10	400	434.0	1578.0
11	600	667.0	2715.1
12	800	913.4	3628.43

Table 3: Dose Information

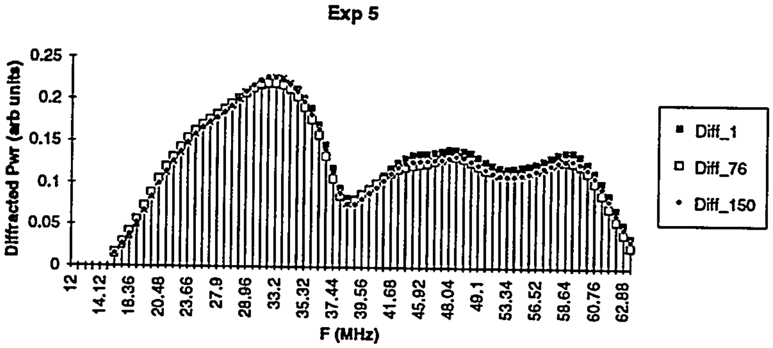

Figure 17: Exposure 5 Plot 2: Traces 76 and 150 were during recovery.

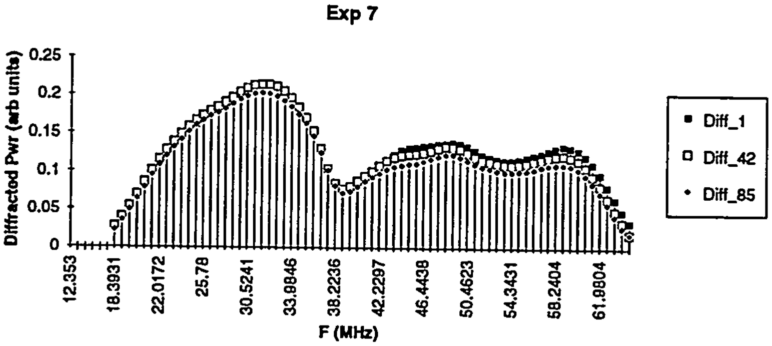

Figure 18: Exposure 7 Plot 1: Traces 1, 42 and 85 were during radiation.

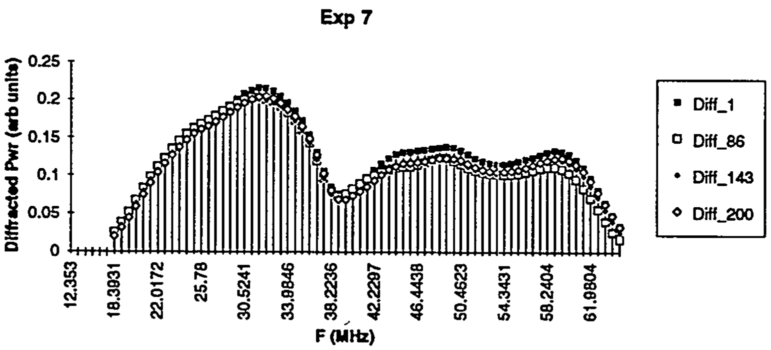

Figure 19: Exposure 7 Plot 2: Traces 86, 143 and 200 were during recovery.

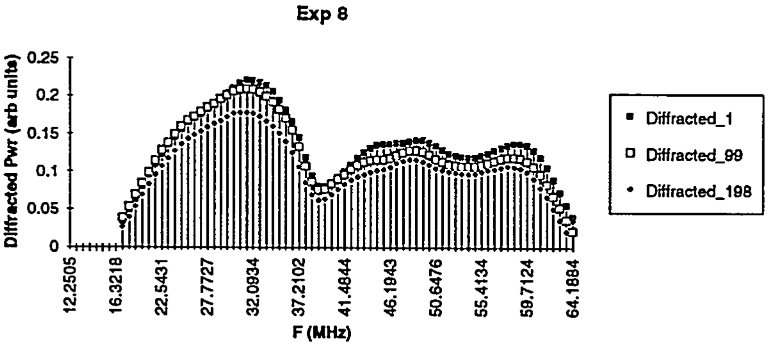

Figure 20: Exposure 8 Plot 1: Traces 1, 99 and 198 were during radiation.

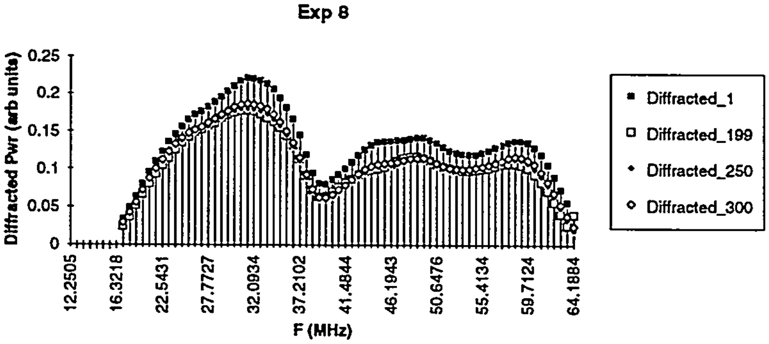

Figure 21: Exposure 8 Plot 2: Traces 199, 250 and 300 were during recovery.

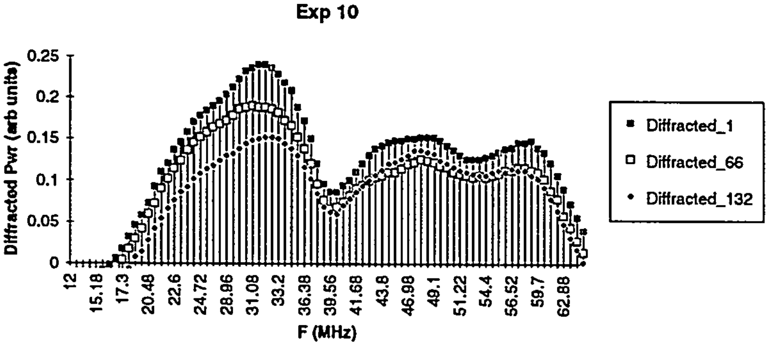

Figure 22: Exposure 10 Plot 1: Traces 1, 66 and 132 were during radiation.

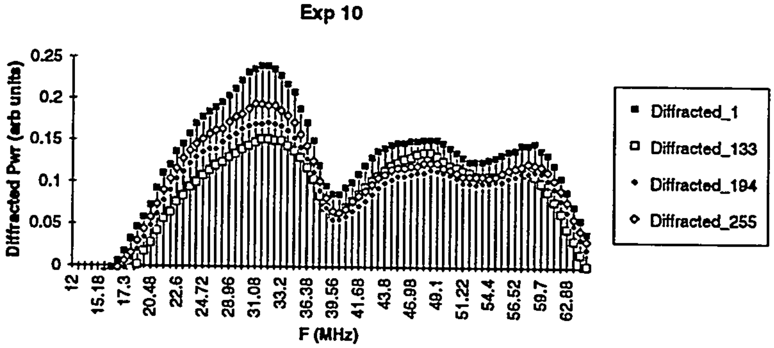

Figure 23: Exposure 10 Plot 2: Traces 133, 194 and 255 were during recovery.

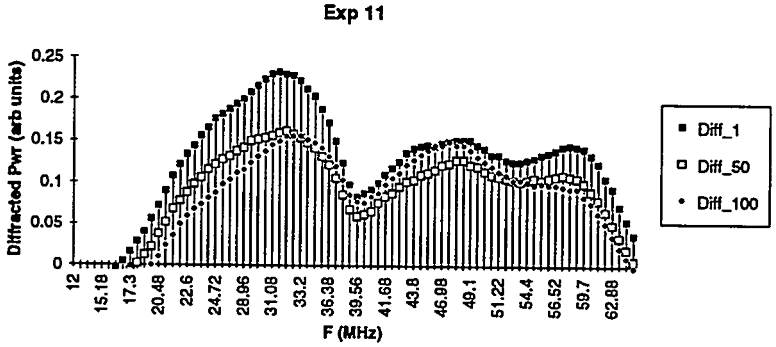

Figure 24: Exposure 11 Plot 1: Traces 1, 50 and 100 were during radiation.

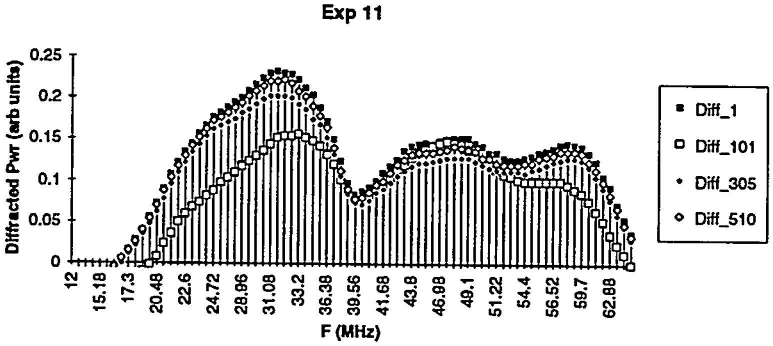

Figure 25: Exposure 11 Plot 2: Traces 101, 305 and 510 were during recovery.

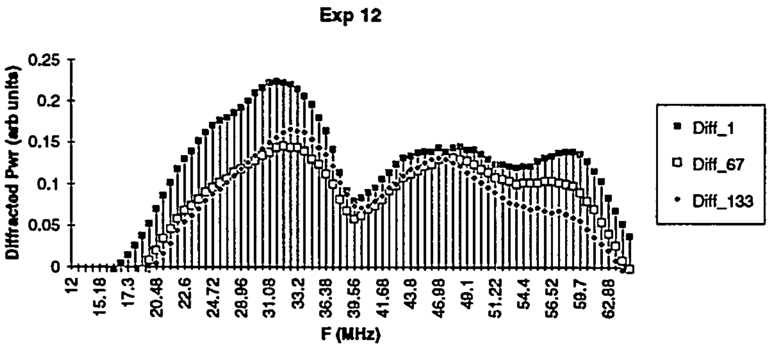

Figure 26: Exposure 12 Plot 1: Traces 1, 67 and 133 were during radiation.

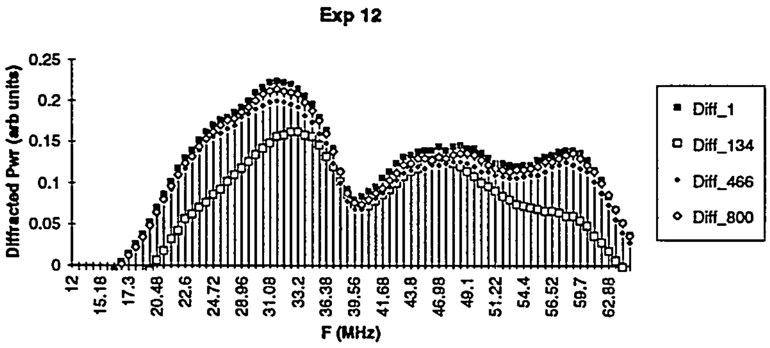

Figure 27: Exposure 12 Plot 2: Traces 134, 466 and 800 were during recovery.

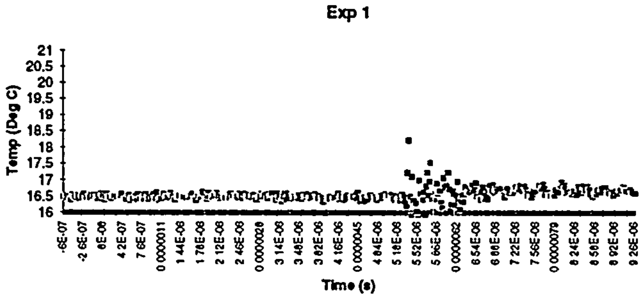

Figure 28: Exposure 1: Temperature vs. Time

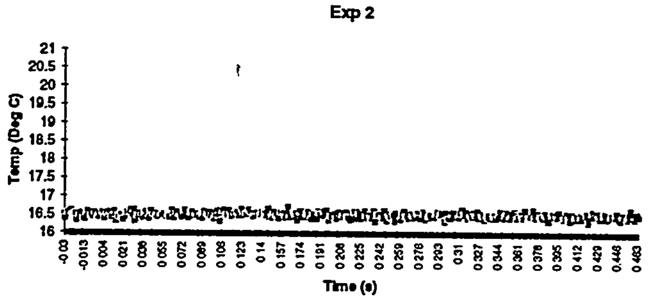

Figure 29: Exposure 2: Temperature vs. Time

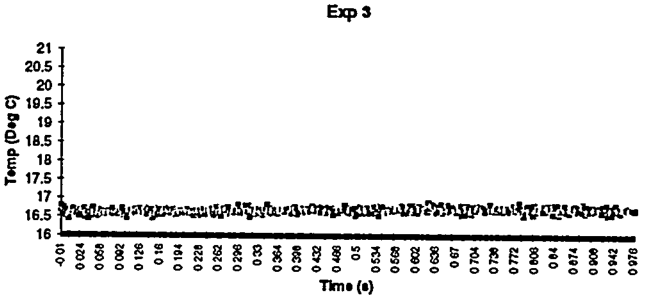

Figure 30: Exposure 3: Temperature vs. Time

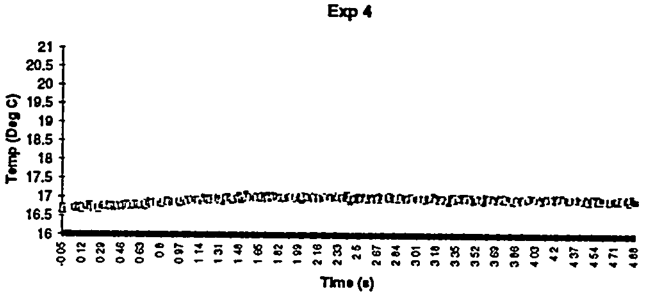

Figure 31: Exposure 4: Temperature vs. Time

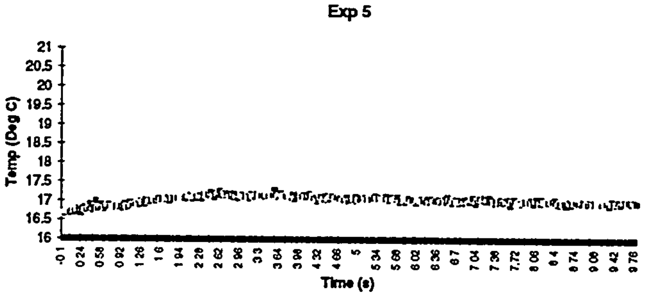

Figure 32: Exposure 5: Temperature vs. Time

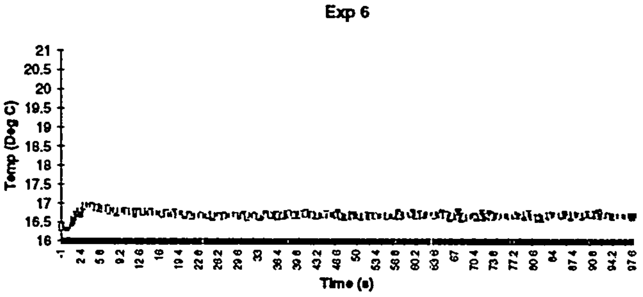

Figure 33: Exposure 6: Temperature vs. Time

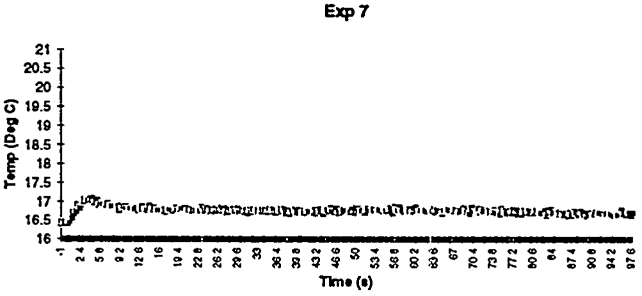

Figure 34: Exposure 7: Temperature vs. Time

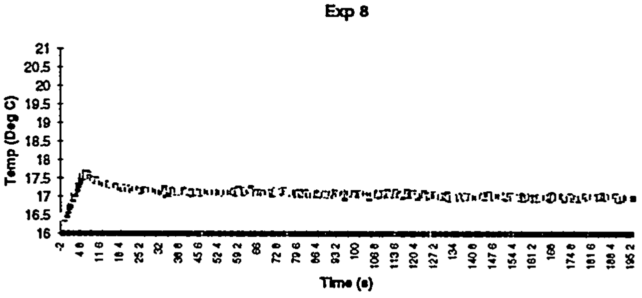

Figure 35: Exposure 8: Temperature vs. Time

5 Discussion

From looking at the data in the previous section, we can make some generalizations about the effect of these levels of radiation on an acousto-optic cell. At low total and cumulative doses, the frequency response bandshape (i.e. diffracted power vs. frequency) remains almost identical during and after radiation. Exposure 4 (95.1 kRad (Si)) is where very slight changes start to be noticed. The accompanying maximum temperature variation for this exposure is 0.4°C. At higher exposures, changes in the bandshape are more noticeable. The frequency response changes as the radiation continues, but returns to the original shape after the radiation stops and recovery proceeds. The temperature data also shows the same type of excursion; the temperature rises as the radiation continues, but starts to return

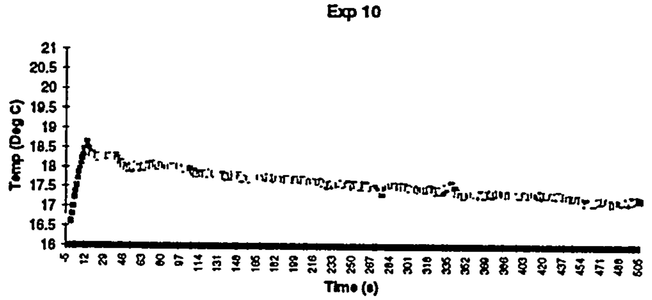

Figure 36: Exposure 10: Temperature vs. Time

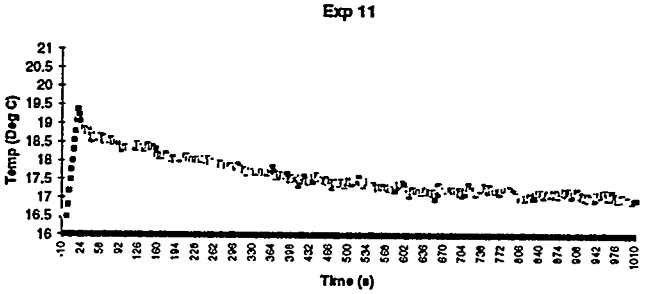

Figure 37: Exposure 11: Temperature vs. Time

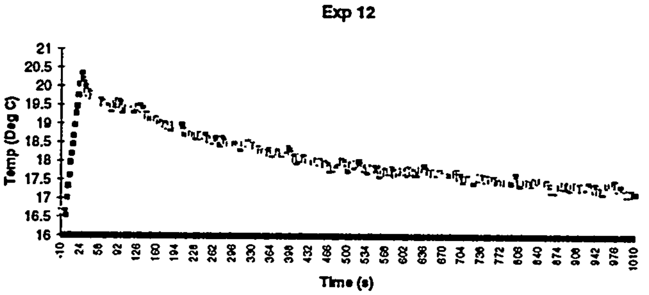

Figure 38: Exposure 12: Temperature vs. Time

back to the original temperature exponentially after the radiation stopped. The maximum change in frequency response bandshape corresponds with the maximum heating.

These observations are qualitative. In the following sections, we try to quantify and explain the phenomenon being observed.

5.1 Location of Bragg Degeneracy

In looking through the frequency response data, we can see that at higher exposures, the amplitude and shape of the diffracted beam power curves change. The frequency location of the Bragg degeneracy is affected by radiation, however not too significantly. In this section, we will see how much of the change in the location of the Bragg degeneracy can be attributed to the change in temperature associated with the radiation.

For our experimental configuration, the angle of rotation of the acousto-optic plane of interaction is small enough that Eqn 10 for f_0 is still valid. In order to see how f_0 is affected by temperature, information is needed on how the velocity of sound varies with temperature and how the indices of refraction vary with temperature.

The effect of temperature on velocity of sound has been studied and presented a number of places. [17, 5] The most recent results are from Dimmick et. al. In their paper [5], they give the temperature coefficient of velocity for the TeO_2 slow shear wave material as 180.6 ppm/°C at T=20°C,

$$\frac{1}{V_a(T)}\frac{dV_a(T)}{dT} = 180.6\frac{ppm}{^\circ C} \tag{49}$$

or

$$\frac{dV_a(T)}{dT} = 180.6\text{x}10^{-6}V_a\left[\frac{m/s}{^\circ C}\right]. \tag{50}$$

$V_a(T)$ at 20° C is 617 m/s, resulting in

$$\frac{dV_a(T)}{dT} = 0.111\left[\frac{m/s}{^\circ C}\right]. \tag{51}$$

For information on the temperature dependence of the indices of refraction, we refer to the paper by Ohmachi and Uchida. [16]. That paper contains plots of the temperature dependence of the complex dielectric constants. Recall that

$$\epsilon^{(1)} = \epsilon^{(2)} = n_o^2 \tag{52}$$

$$\epsilon^{(3)} = n_e^2. \tag{53}$$

From the plots, we extrapolate the following temperature coefficients:

$\epsilon_{33}(0°) = 1/7 * 4.5 + 24 = 24.64$
$\epsilon_{33}(50°) = 1/7 * 6.5 + 24 = 24.93$
$\Rightarrow 0.006/°C$ for ϵ_{33}

$\epsilon_{11}(0°) = 1/7 * 6 + 22 = 22.86$
$\epsilon_{11}(50°) = 1/7 * .5 + 23 = 23.07$
$\Rightarrow 0.004/°C$ for ϵ_{11}.

With this information, we now can calculate the ratio of $\frac{f_0(B)}{f_0(A)}$, where $B = 20.2°C$ is the temperature at the location of maximum shift in location of Bragg degeneracy, and $A = 16.5°C$ is the steady state temperature in Exposure 12.

The complex dielectric constants are linear with temperature in our range of interest. [16] In order to calculate $\frac{f_0(B)}{f_0(A)}$, we are interested in the change of $(n_1^2 - n_2^2)$ with temperature over the range A to B. Therefore it is reasonable to calculate the values of $n_1^2(B) - n_2^2(B)$ and $n_1^2(A) - n_2^2(A)$ to the same number of significant digits as the temperature coefficients of the dielectric constants, even though the absolute values are not known to that significance.

From Reference [16], at $20°C$,

$$n_1^2 = 24.7 \tag{54}$$

$$n_2^2 = 22.9. \tag{55}$$

Using the complex dielectric constants temperature coefficients calculated above, we get

$$n_1^2(16.5°) = 24.679 \tag{56}$$

$$n_2^2(16.5°) = 22.886, \tag{57}$$

and

$$n_1^2(20.25°) = 24.701 \tag{58}$$

$$n_2^2(20.25°) = 22.871. \tag{59}$$

Using the temperature coefficient of velocity, we get

$$V(B) = V(A) + 0.111\frac{m/s}{°C}(B - A) \tag{60}$$

or

$$\frac{V(B)}{V(A)} = 1 + \frac{3.7(.111)}{617} = 1.0007. \tag{61}$$

Finally,

$$\frac{f_0(B)}{f_0(A)} = \frac{V(B)}{V(A)}\frac{\sqrt{n_1^2(B) - n_2^2(B)}}{\sqrt{n_1^2(A) - n_2^2(A)}}$$

$$= (1.0007)\sqrt{\frac{1.830}{1.793}} = 1.01. \tag{62}$$

For actual results, we look to Figure 27. From the figure, $f_0(B) = 40.02$ MHz and $f_0(A) = 39.60$ MHz, giving $\frac{f_0(B)}{f_0(A)} = 1.01$. The calculated and actual results are remarkably close. To within the precision available, the change in location of the Bragg degeneracy can be attributed in its entirety to the change in temperature.

5.2 3-dB Bandwidth of the Diffracted Beam Intensity

In looking at the plots of the diffracted beam intensity vs. frequency, it is hard to discern the effect on the bandwidth. By bandwidth, we mean the span of frequency over which the diffracted power remains within a certain tolerance, usually 3-dB. At low radiation exposures, basically no change is noticed at all. At higher exposures, however, the amplitude of the diffracted power is reduced. This reduction is more prominent at the very low and very high frequency regions. At the highest exposures, the magnitude of the ripple is reduced, and it appears that the bandwidth is reduced slightly also.

Once again, we would like to see if the reduction in bandwidth observed is consistent with the change in bandwidth due to thermal expansion for the temperature change observed in these experiments.

Recall earlier, we gave an equation describing the intensity of the diffracted beam for an AO deflector, Eqn 40. For the appropriate optical rotation in the birefringent case, the phase mismatch is given by Eqn 43. To find the 50% bandwidth, δ_1 is set to 0.45. Recalling that $F = \frac{f}{f_o}$, and therefore the complete bandwidth, Δf, is double what is given by setting $\delta_1 = 0.45$, we arrive at

$$\left.\frac{\Delta f}{f_o}\right|_T = \sqrt{\frac{3.6L_o}{L(T)}}. \tag{63}$$

From Reference [16], the thermal expansion coefficients are

$$\alpha_1 = 20\text{x}10^{-6}/^\circ C \tag{64}$$

$$\alpha_3 = 6.6\text{x}10^{-6}/^\circ C. \tag{65}$$

Assuming the crystal is oriented so that interaction length is along α_1, then

$$\frac{\left.\frac{\Delta f}{f_o}\right|_B}{\left.\frac{\Delta f}{f_o}\right|_A} = \frac{1}{\sqrt{1+\alpha_1(\Delta T)}}, \tag{66}$$

where definitions for A and B are the same as in the previous section. For data from Exposure 12, $\Delta T = 3.7$, and

$$\frac{\left.\frac{\Delta f}{f_o}\right|_B}{\left.\frac{\Delta f}{f_o}\right|_A} = 0.99996 \tag{67}$$

To appropriate precision, there is no change in 3-dB bandwidth due to the thermal expansion for this small change in temperature.

The change in amplitude observed, however, appears more significant. Recall that the amplitude of the intensity is given by $I_{1p} = \sin^2(\frac{v}{2})$, where $\left(\frac{v}{2}\right)^2 = \frac{\pi^2}{2\lambda_0^2} M_2 \frac{P_a L}{H \cos^2 \theta_0}$. This shows the relationship between the acoustic power and amplitude of the intensity, I_{1p}. We need to consider the effect of radiation on the acoustic power. Changes in 3-dB bandwidth may be attributed to a change in acoustic power and/or acoustic attenuation.

It is well known that the acoustic attenuation for a crystal like TeO_2 is proportional to the frequency squared, $\alpha = \alpha_0 f^2$. [22, 24] Consequently, if the acoustic attenuation constant, α_0, increases, the higher frequency components will be attenuated more and the bandwidth will decrease. We will discuss this more in the following section.

5.3 Bandshape of the Diffracted Beam Intensity vs. Frequency

It can be seen that the bandshape of the frequency response changes with radiation. Qualitatively, the changes can be described as follows:

- The overall diffraction efficiency (diffracted power) is reduced.
- The reduction of diffracted power varies with frequency. The difference between the diffracted power in the low frequency peak and the high frequency peak decreases.
- Through Exposure 8, as one would expect, with more radiation, the diffracted power was uniformly lower than without radiation for all frequencies. At Exposure 10, the performance is slightly better at higher frequency with higher radiation exposure. By looking at Figure 22, the two peaks are approaching the same height. At Exposure 11, at maximum radiation, the two peaks are virtually identical in height, and the degeneracy dip has decreased. At Exposure 12, the low frequency peak increased to be once again higher than the high frequency peak. At Exposures 11 and 12, a severe rolloff at highest frequencies is seen.

The fact that the overall diffracted power is reduced by the radiation leads us to believe that the acoustic power is affected by the radiation. Since the acoustic power being delivered to the crystal was constant for the experiment, and care was taken to isolate the radiation only to the crystal, this drop in the acoustic power should be a result of something other than transducer effects. Possible mechanisms are acoustic coupling, acoustic reflection (the reflection caused upon the acoustic wave impinging on an area of increased refractive index, due to increased temperature), and acoustic attenuation.

No published measurements for slow shear [110] TeO_2 exist detailing the effect of temperature on acoustic attenuation, so we cannot determine if the effects observed are due to the temperature rise in the crystal or due to a direct radiation effect.

Previously, we gave equations governing the diffracted beam intensity.

$$I_1 = I_{1p}\text{sinc}^2\left(\frac{\Delta k_1 L}{2}\right),$$

where

$$I_{1p} = \sin^2\left(\frac{v}{2}\right)$$

and

$$\left(\frac{v}{2}\right)^2 = \frac{\pi^2}{2\lambda_0^2}\frac{n^6p^2}{\rho V^3}\frac{P_a L}{H\cos^2\theta_0}.$$

The term $\left(\frac{v}{2}\right)^2$ can be considered the acoustic drive power. From these equations, it is clear that if $\left(\frac{v}{2}\right)^2$ decreases, the coefficient, I_{1p} will decrease, and the overall diffracted beam intensity will decrease. It is clear that other physical parameters in the equation for $\left(\frac{v}{2}\right)^2$ are functions of temperature, however, the variations of these parameters are relatively small [16] and collectively would tend to increase the value of $\left(\frac{v}{2}\right)^2$ with an increase in temperature. It would be beneficial to study the acoustooptic figure of merit, M_2, as a function of temperature.

The variation of P_a with temperature is unknown. Data indicates that the acoustic drive power, $\left(\frac{v}{2}\right)^2$, does decrease with radiation, hence we can conclude that P_a decreases with radiation, although it is not clear through which mechanism.

The acoustic power level has a significant impact on the uniformity of deflected power over a frequency band. First, the acoustic power level determines how much power is coupled into the degenerate mode at f_o. This is clear from coupled mode theory covering the three modes. [25] If the three modes are: a_1, the incident slow mode; a_2, the deflected fast mode; and a_3, the degenerate mode, then their coupling over a distance z can be described by

$$j\frac{da_n}{dz} = \sum_{n=1}^{3} H_{nm}a_m, \tag{68}$$

$n, m = 1, 2, 3$ and $H_{nm} = H_{mn}$. H_{nm} are the coupling coefficients between modes.

When all modes are phase matched, i.e. at $f = f_o$,

$$H_{11} = H_{22} = H_{33} = k_0$$

$$H_{13} = 0$$

$$H_{12} = H_{23} \propto P_a\mathcal{P}, \tag{69}$$

where $\mathcal{P}$ is the acousto-optic coupling constant.

Solution has the form of an exponential in z, $A\exp(j\beta z)$, with eigenvalues $\beta_1 = H_{11}$ and $\beta_2 = H_{11} \pm \sqrt{2}H_{12}$. The results are

$$a_1(z) = \frac{1}{2}a_0(1 + \cos\sqrt{2}H_{12}z)\exp(-jH_{11}z) \tag{70}$$

$$a_2(z) = \frac{a_0}{\sqrt{2}}(\sin\sqrt{2}H_{12}z)\exp(-jH_{12}z) \tag{71}$$

$$a_3(z) = \frac{1}{2}a_0(-1 + \cos\sqrt{2}H_{12}z)\exp(-jH_{12}z). \tag{72}$$

The corresponding power flow is

$$P_1 = \frac{1}{4}P_0(1 + \cos^2\sqrt{2}H_{12}z + 2\cos\sqrt{2}H_{12}z) \tag{73}$$

$$P_2 = \frac{1}{2}P_0(\sin^2\sqrt{2}H_{12}z) \tag{74}$$

$$P_3 = \frac{1}{4}P_0(1 + \cos^2\sqrt{2}H_{12}z - 2\cos\sqrt{2}H_{12}z), \tag{75}$$

where

$$P_0 \propto a_0 a_0^*. \tag{76}$$

When the modes are not phase matched, $H_{23} = 0$, giving

$$P_1 = P_0\cos^2 H_{12}z \tag{77}$$

$$P_2 = P_0\sin^2 H_{12}z. \tag{78}$$

Remember that H_{12} is proportional to the amplitude of the acoustic wave and the acousto-optic coupling coefficient. At low acoustic power, $\sqrt{2}H_{12}z \ll 1$, making P_3 negligible to P_2.[1] This is seen in Figure 5.3. The dashed curve represents P_3, the power in the degenerate mode. The solid curve represents P_2, the power in the desired deflected mode. From the figure, we see that the deflected power is more uniform over the degeneracy at low power.

At higher acoustic power, it is clear that P_3 becomes significant compared to P_2. In Figure 5.3, there are three curves plotted. The finely dashed curve represents the power in the deflected mode, when *not* at the degenerate frequency. The other two curves are the same as in Figure 5.3, at the degenerate frequency. It is clear that as power increases, there is a drop in the power in the deflected mode at the degenerate frequency. Therefore, at higher P_a, the degeneracy dip in the middle of the frequency span is more significant.

The acoustic power affects uniformity of the deflected power in another way. Consider the efficiency vs. drive power in Figure 5.3.[2] The family of curves are for various values of fractional bandwidth, $\frac{\Delta f}{f_0} = 0, 0.25, 0.5$. From this plot, there are several interesting things to note:

---

[1] $P_3 = \mathcal{O}(\sqrt{2}H_{12}z)^4$; $P_2 = \mathcal{O}(\sqrt{2}H_{12}z)^2$

[2] Note: This plot has been incorrectly presented a number of places. [28, 2] In these places, Eqn 34 is not plotted. Instead, $\left(\frac{v}{2}\right)^2 \frac{\sin^2\sigma}{\sigma}$ was plotted.

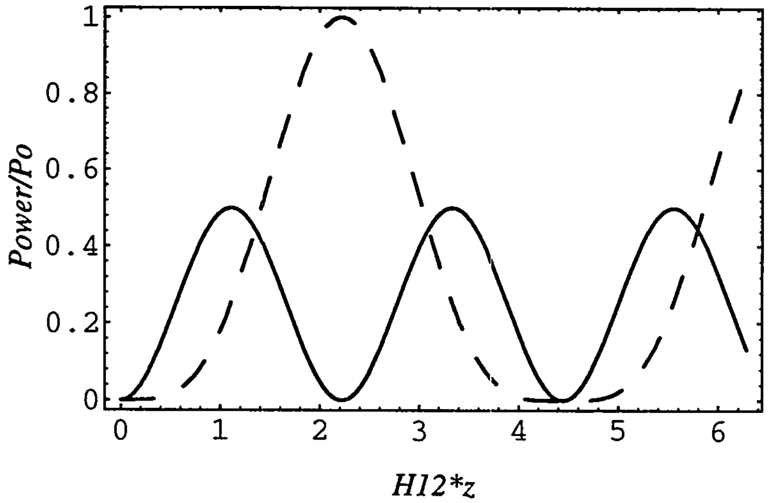

Figure 39: Power in the Deflected Mode (solid) and Degenerate Mode (dashed) at the Degenerate Frequency.

1. The efficiencies for all curves are the closest in value for small values of $\left(\frac{v}{2}\right)^2$. This means that at low normalized power, the bandshape is relatively flat.
2. Efficiency (diffracted power) can be increased by increasing the drive power, but as the drive power increases, so does the difference in diffracted power at low versus high frequencies. Furthermore, consider the peaks of the diffracted power for different fractional bandwidths. Let DP_0 be the drive power where the diffracted power for the 0% fractional bandwidth peaks. Similarly, let DP_{25} and DP_{50} be the drive powers corresponding to the 25% and 50% fractional bandwidth peaks, respectively. Initially as the drive power increases from 0, all the diffracted powers increase, but the power for the lower fractional bandwidths increases more than for the higher fractional bandwidths. For drive power, DP, in the range $DP_0 > DP > DP_{50}$, the diffracted power in the 25% and 0% fractional bandwidths increase as DP increases, but the diffracted power in the 50% fractional bandwidth decreases. The result is that in this range, the bandwidth and uniformity decrease as the drive power increases. Eventually for $DP > DP_{50}$, all efficiencies decrease with increasing DP, but the bandshape again becomes more uniform.

A final point should be considered when looking at the bandshape of the frequency response. As has been mentioned, it is well known that the acoustic attenuation

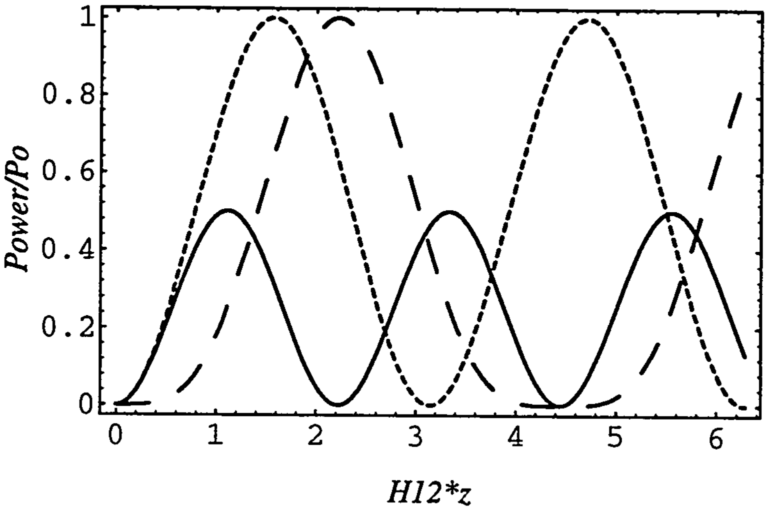

Figure 40: Power in the Deflected Mode at Degeneracy (solid). Power in the Degenerate Mode at Degeneracy (coarsely dashed). Power in the Deflected Mode *not* at Degeneracy (finely dashed).

is proportional to the square of frequency. This accounts for the fact that without radiation, the lower frequency peak is higher than the higher frequency peak. If the attenuation increases with radiation, this also explains that as the radiation increases, the upper frequency portion of the bandshape starts rolling off at lower and lower frequencies. This is especially noticeable in Exposures 10, 11 and 12.

5.4 Recovery from Effects

The exposures in this experiment ranged from 2.25 kRad (Si) to 913 kRad (Si). All of the effects we have discussed appear to be transient, i.e. not permanent. It is clear that after the radiation pulses stop, the frequency response starts to go back to its original characteristics. Although data was not always taken out to the time of complete recovery, complete recovery did occur between runs. The temperature recovery corresponds to the frequency response recovery.

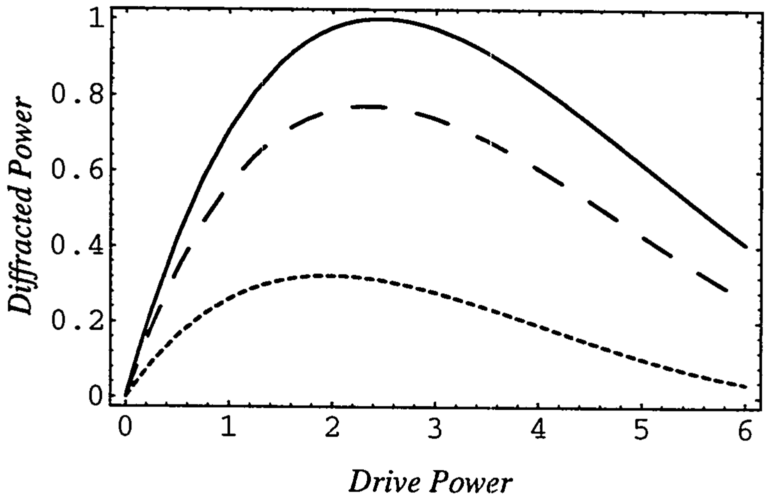

Figure 41: Efficiency (Diffracted Power) vs. Drive Power for Fractional Bandwidth 0% (solid), 25% (coarsely dashed) and 50% (finely dashed).

5.5 Effect on Signal Processing Functions

It is interesting to see in the previous sections how radiation affects the frequency response of an acousto-optic cell, but the critical issue is how the signal processing performance is affected when the AO cell is used in an optical processing system. More specifically, we are interested in how the performance of an AO spectrum analyzer will be affected by radiation.

For most AO processing systems, a critical parameter is the time bandwidth product (TBWP) of the AO cell. The TBWP can be thought of as the information capacity of the cell, and hence the system. Equivalently, the TBWP is the number of resolvable elements. By resolvable elements, we mean either the number of resolvable frequencies in a fourier transform plane or the number of resolvable elements in an image plane. The TBWP is determined by the maximum duration and bandwidth signal on which the device can properly operate. An increase in TBWP means either an increase in interaction time, an increase in interaction bandwidth, or both.

In the previous sections, we have seen how a variety of physical parameters are affected by radiation or temperature. These parameters, in turn, affect the TBWP and hence the performance of an AO processing system.

Recall, that as the cell is irradiated, it heats up. Consequently, the acoustic velocity increases. This increase in V will limit τ, the transit time across the cell, and hence the TBWP. Recall $\tau = D/V$, where D is the cell aperture.

In addition, we can see that with radiation, acoustic power decreases. One possible cause of this is increased acoustic attenuation with temperature or with radiation. An increase in attenuation limits the allowable cell aperture, and hence also limits τ.

In applications where the speed of the device is not of major concern, the resolution is limited by either the physical constraint of the optical aperture or the acoustic attenuation, α, at high frequency. Both these items serve to limit D. (If speed is of concern, that too limits D, usually more so than the physical constraint or acoustic attenuation.) For most crystalline solids, the acoustic attenuation is proportional to the frequency squared, $\alpha = \alpha_0 f^2$. If the maximum attenuation tolerated is $\mathcal{L}$ (dB), then the maximum allowed transit time would be $\frac{\mathcal{L}}{\alpha_o f_{max}^2}$. Consequently, the maximum TBWP, N_{max} is given by

$$N_{max} = \frac{\mathcal{L}\Delta f}{\alpha_o f_{max}^2}. \tag{79}$$

It is clear that if the acoustic attenuation increases, with either temperature or radiation, the maximum number of resolvable points decreases accordingly.

Work must be done to investigate acoustic attenuation and acoustic absorption. Acoustic absorption vs. temperature for shear [100] has been presented. [16] Indeed there is an increase with temperature, of about $\frac{1}{150}\frac{dB/cm}{°C}$, but this cannot be guaranteed to occur or at what magnitude for shear [110]. If decreased acoustic power can be attributed solely to the increase in temperature, then temperature stabilization can be used to take care of the limits imposed from increased acoustic velocity, absorption and attenuation on the TBWP. If the decrease in acoustic power cannot be attributed to increased temperature alone, then even with temperature stabilization, the TBWP will decrease, and the processing capacity will be reduced with radiation.

Temperature stabilization has already been shown to be necessary for acousto-optic spectrum analyzers. [5] The acoustic velocity has a direct effect on frequency resolution,

$$\Delta f = \frac{sV_a}{\lambda F},$$

where s is the spacing between detectors in the detector array, and F is the focal distance of the lens. For a TeO_2 cell (slow shear mode [110]), with bandwidth of 60MHz, center frequency of 90MHz, and time aperture of $70\mu s$, it was shown that temperature must be stabilized to within $0.328°C$ to maintain the highest TBWP (N=4200). If the detector spacing is relaxed and the full TBWP is not utilized, the ΔT restrictions can be lessened. For N=1000, $\Delta T < 1.39°C$.

Finally if the magnitude of the signal at a given frequency is important, not just detection, then some sort of compensation or equalization is typically required. This type of compensation is commonly done using electronic pre- or post-processing. If it is known that the bandshape may vary and the various bandshapes are known a priori, it wouldn't be difficult to incorporate this into the electronic compensation. Of course, all the electronic processing would be implemented using hardened components. From the data, it seems the magnitude of the signal at $\approx$ 32MHz could be used as an indication of what bandshape compensation to use. A test signal at 32MHz can be periodically injected, and the resulting signal value could be used to pick the appropriate compensation.

6 Conclusions and Future Work

In this report, we presented the results of an experiment designed to show the effect of space-level radiation[3] on the frequency response of a TeO_2 slow shear acousto-optic cell. The goals were to observe what kinds of changes took place, to try to find the mechanisms responsible for the changes observed, and to relate these changes to overall system performance.

At low total and cumulative doses, the frequency response bandshape remained almost identical during and after radiation. Slight changes began to be noticed at a dose of 95.1 kRad (Si) and got larger with increasing dose. The frequency response changed as the radiation continued, but returned to the original shape after the radiation stopped and recovery proceeded. Accompanying the radiation and changes in frequency response was an increase in temperature.

The changes in frequency response can be broken into three parts: (1) the location of the Bragg degeneracy; (2) the 3-dB bandwidth of the diffracted beam intensity; and (3) the bandshape of the diffracted beam intensity.

These three items were investigated thoroughly in this report in an attempt to determine the mechanisms that cause changes in them with radiation. The change in location of the Bragg degeneracy can be attributed entirely to the increase in temperature of the cell with radiation. The change in 3-dB bandwidth due to thermal expansion is virtually non-existent. Consequently, changes in 3-dB bandwidth are attributed to a change in acoustic power and/or acoustic attenuation. The changes in bandshape can also be attributed to changes in acoustic drive power and acoustic attenuation. Because no material studies have been done to establish the dependence of acoustic power or acoustic attenuation on temperature, it cannot be determined if the changes are due to the radiation itself, or the temperature rise due to radiation. This must be studied further. It is also curious that for the highest dose exposure, Exposure 12, at the last radiation pulse, the low frequency peak diffracted power actually increased over its values with less radiation. This needs to be studied further.

The observed changes in frequency response were then related to system perfor-

---

[3] total integrated dose $< 5 \times 10^6$ rad (Si)

mance. Though the magnitude of changes do not appear that great, they do impact the performance achievable with acousto-optic processing systems. The effects observed will result in a reduced TBWP for the system. A reduced TBWP reduces the information processing capacity of a system, but the system can still perform.

An acousto-optic processing system operating in space must be designed so that it can perform within certain tolerances (i.e. changes in temperature must be within a given range, acoustic power, P_a, must be within a given range, acoustic attenuation must be within a given range, etc.). These restrictions will limit the processing capacity (or resolution), but provide a margin of safety for known correct operation under these conditions.

References

[1] M. Amano, G. Elston, and J. Lucero. Materials for large time aperture Bragg cell. *SPIE Proceedings*, 567:141–149, 1985. Advances in Materials for Active Optics.

[2] N. Berg and J. Lee, editors. *Acoutsto-optic Signal Processing: Theory and Implementation.* Dekker, 1983.

[3] I. Chang. Acoutooptic devices and applications. *IEEE Transactions on Sonics and Ultrasonics*, SU23(1):2–22, January 1976.

[4] P. Das and C. DeCusatis. *Acousto-optic Signal Processing: Fundamentals and Applications.* Artech House, 1991.

[5] T. Dimmick, D. Satorius, and J. Fewer. Temperature sensitivity of acoustic velocity and frequency registration in acousto-optic spectrum analyzers. *Applied Optics*, 31(14):2409–2411, 10 May 1992.

[6] R. Dixon. Acoustic diffraction of light in anisotropic media. *IEEE Journal of Quantum Electronics*, QE-3(2):85–93, February 1967.

[7] G. Elston. Optically and acoustically rotated slow shear bragg cells in TeO_2. Technical report, Crystal Technology Incorporated, 1986.

[8] G. Elston, M. Amano, and J. Lucero. Material tradeoff for wideband Bragg cells. *SPIE Proceedings*, 567:150–158, 1985. Advances in Materials for Active Optics.

[9] G. Elston and P. Kellman. The effects of acoustic nonlinearities in acousto-optic signal processing systems. Technical report, ESL Incorporated, 495 Java Drive, Sunnyvale, CA 94088-3510.

[10] E. Gordon. A review of acoustooptical deflection and modulation devices. *Applied Optics*, 5(10):1629–1639, October 1966.

[11] M. Gottlieb, C. Ireland, and J. Ley. *Electro-optic and Acousto-optic scanning and Deflection.* Decker, 1983.

[12] D. Hecht. Spectrum analysis using acoutso-optic devices. *SPIE Proceedings*, 90:148–157, 1976. Acousto-Optics.

[13] B. Javidi and J. Horner, editors. *Real-Time Optical Information Processing*. Academic Press, 1994.

[14] A. Korpel. *Acousto-optics*. Dekker, 1988.

[15] K. McCarthy and H. Sample. Thermal conductivity of a fluorozirconate glass and tellurium dioxide single crystals. *14th Annual Symposium on Optical Materials for High Power Lasers*.

[16] Y. Ohmachi and N. Uchida. Temperature dependence of elastic, dielectric and piezoelectric constants in TeO_2 single crystals. *Journal of Applied Physics*, 41(6):2307–2311, May 1970.

[17] Y. Ohmachi and N. Uchida. Acoustic and acousto-optical properties of TeO_2 single crystal. *Review Electronic Communications Lab*, 20:529–541, 1972.

[18] J. Pellegrino, L. Harrison, and N. Berg. Ruggedization and miniaturization of real-time acousto-optic correlators and spectrum analyzers. *SPIE Proceedings*, 639:160–166, 1986. Optical Information Processing II.

[19] P. Phariseau. On the diffraction of light by progressive supersonic waves. *Proceedings of the Indian Academy of Sciences*, 44A:165–170, October 1956.

[20] J. Rouvaen, M. Ghazaleh, E. Bridoux, and R. Torguet. On a general treatment of acousto-optic interactions in linear anisotropic crystals. *Journal of Applied Physics*, 50(8):5472–5477, August 1979.

[21] M. Shah and D. Pape. A generalized theory of phased array Bragg interaction in a birefringent medium and its application to TeO_2 for intermodulation product reduction. *SPIE Proceedings*, 1704:210–220, 1992. Advanced in Optical Information Processing V.

[22] N. Uchida. Acoustic attenuation in TeO_2. *Journal of Applied Physics*, 43(6):2915–2917, June 1972.

[23] N. Uchida and N. Niizeki. Acoustooptic deflection materials and techniques. *Proceedings of the IEEE*, 61(8):1073–1092, August 1973.

[24] N. Uchida and Y. Ohmachi. Elastica and photoelastic properties of TeO_2 single crystal. *Journal of Applied Physics*, 40(12):4692–4695, November 1969.

[25] A. Warner, D. White, and W. Bonner. Acousto-optic light deflectors using optical activity in paratellurite. *Journal of Applied Physics*, 43(11):4489–4495, November 1972.

[26] J. Xu and R. Stroud. *Acousto-Optic Devices: Principles, Design and Applications*. J. Wiley and Sons, 1992.

[27] T. Yano, M. Kawabuchi, A. Fukumoto, and A. Watanabe. TeO_2 anisotropic Bragg light deflector without midband degeneracy. *Applied Physics Letters*, 26(12):689–691, June 1975.

[28] E. Young and S. Yao. Design considerations for acousto-optic devices. *Proceedings of the IEEE*, 69(1):54–64, January 1981.

DISTRIBUTION:

2 Defense Nuclear Agency
Attn: Major Ron Doby
Electronic Effects Division (RAEE)
6801 Telegraph Road
Alexandria, VA 22310

1	MS 9018	Central Technical Files, 8523-2
5	MS 0899	Technical Library, 13414
1	MS 0619	Print Media, 12615
2	MS 0100	Document Processing, 7613-2 For DOE/OSTI